

VĚDECKÉ SPISY VYSOKÉHO UČENÍ TECHNICKÉHO V BRNĚ

*Edice PhD Thesis, sv. 749*

*ISSN 1213-4198*

*thesis* IS

*Ing. Hana Druckmüllerová*

**Application of Adaptive Filters  
in Processing of Solar Corona Images**

VYSOKÉ UČENÍ TECHNICKÉ V BRNĚ  
FAKULTA STROJNÍHO INŽENÝRSTVÍ  
ÚSTAV MATEMATIKY

**Ing. Hana Druckmüllerová**

**APPLICATION OF ADAPTIVE FILTERS IN PROCESSING  
OF SOLAR CORONA IMAGES**

**APLIKACE ADAPTIVNÍCH FILTRŮ  
PŘI ZPRACOVÁNÍ SNÍMKŮ SLUNEČNÍ KORÓNY**

Zkrácená verze Ph.D. Thesis

Obor: Aplikovaná matematika  
Školitel: doc. PaedDr. Dalibor Martišek, Ph.D.  
Oponenti: RNDr. Vojtech Rušin, DrSc.  
prof. RNDr. Ivanka Horová, CSc.  
Datum obhajoby: 2. června 2014

**Keywords**

solar corona, adaptive filters, image processing, Fourier normalizing-radial-graded filter.

**Klíčová slova:**

sluneční koróna, adaptivní filtry, zpracování obrazů, Fourier normalizing-radial-graded filter.

**Rukopis dizertační práce je uložen**

v Areálové knihovně Fakulty strojního inženýrství  
Vysokého učení technického v Brně.

© Hana Druckmüllerová, 2014

ISBN 978-80-214-4998-5

ISSN 1213-4198

# Contents

<b>1</b>	<b>Introduction</b>	<b>5</b>
<b>2</b>	<b>Imaging the solar corona</b>	<b>6</b>
2.1	The solar corona . . . . .	6
2.2	Imaging possibilities for the solar corona . . . . .	6
2.3	Methods of compensation for the brightness gradient . . . . .	8
<b>3</b>	<b>Fourier normalizing-radial-graded filter</b>	<b>9</b>
3.1	Normalizing-radial-graded filter . . . . .	9
3.2	The principle of the filter . . . . .	10
3.2.1	The basic idea of the filter . . . . .	10
3.2.2	Attenuation coefficients . . . . .	14
3.2.3	Influence of additive noise . . . . .	17
3.3	Results . . . . .	19
3.3.1	Application to total solar eclipse observations . . . . .	19
3.3.2	Application to space-based observations . . . . .	21
3.3.3	Comparison with other methods . . . . .	22
3.4	Software implementation . . . . .	25
<b>4</b>	<b>Conclusion</b>	<b>27</b>
	<b>Bibliography</b>	<b>28</b>
	<b>Curriculum vitae</b>	<b>31</b>



# 1 Introduction

The Sun is the nearest star to the Earth, therefore the research of the Sun gives mankind a unique opportunity to study the physical parameters and properties of a star. The intensity and the spectral composition of the light emitted by the Sun as well as other particles that escape from the Sun play a vital role for the life on Earth. Since people are using more and more complicated electronic devices both on the Earth and in Space and some of these devices are connected in large (global) networks, it is necessary to understand how and when the phenomena on the Sun can harm them.

A very nice popular-scientific article on the danger of a massive solar flare including information about the March 1989 flare can be found in [dGre12]. A scientific article on this topic is given for instance in [cSta02]. Current electronic devices are even more sensitive than those in 1989.

Among the methods of the solar corona research, imaging methods play a crucial role. Due to the problems described in Chapter 2, sophisticated image processing techniques are necessary for taking full advantage of the current mechanical and optical systems for both Earth-based and space-born observations. Among them is the Normalizing-radial-graded filter (NRGF), which was the inspiration for the Fourier normalizing-radial-graded filter (FNRGF) proposed, implemented, and tested on many types of data as part of my Ph.D. study and described in Chapter 3. The filter brings new possibilities for studying the corona, some faint structures are enhanced better than with any of the previous methods. Chapter 3 contains the principle of the filter and many examples of images processed with this filter. Chapter 4 is the Conclusion, followed by the Bibliography, author's CV and the abstract.

# 2 Imaging the solar corona

## 2.1 The solar corona

The Sun can be divided into the interior and the atmosphere. The interior consists of the core, which is the source of the Sun's energy, the place where hydrogen is transformed to heavier elements in thermonuclear reactions, the radiative zone, where energy is transmitted by radiation, and the convective zone. The Sun's magnetic field has its origin in the transition layer between the radiative and the convective zone. The tops of the convective cells form a layer called the photosphere, which is also the border between the interior and the Sun's atmosphere. We often refer to the interior and the photosphere as 'the Sun', since the edge is clearly defined. The photosphere is what we see when we look at the Sun during a sunny day (with a suitable filter, otherwise we would risk damaging our eyes).

The solar atmosphere, which is above the photosphere, has only a fuzzy transition to the interplanetary space. The solar atmosphere comprises the chromosphere, the transition region, the corona, and the heliosphere. The chromosphere is a thin layer of variable thickness containing mainly neutral hydrogen.

Since the corona is composed of mainly of charged particles, the features that are visible in the corona from the extra-ultraviolet part of the spectrum to the infrared are driven by the magnetic field that is generated in the convection zone. The corona is extremely faint relative to the visible disk of the Sun, having a maximum brightness ratio of  $\approx 1 : 10^6$ , decreasing to  $\approx 10^6$  within a single diameter away from the visible limb [cGoP10]. This is the reason why the corona cannot be observed directly from the Earth without any special instruments – that it is too faint next to the bright photosphere. Section 2.2 is devoted to the possibilities that we have to observe the corona. An example of an image of the inner corona observed in the ultraviolet part of the spectrum can be found in Figure 2.1.

## 2.2 Imaging possibilities for the solar corona

Total solar eclipses have been providing unique opportunities for exploring the properties of the plasma in the inner corona, since the photosphere, which is about one million times as bright as the inner corona, is obscured by the Moon and the sky brightness is significantly reduced. The invention of the coronagraph by Bernard Lyot in 1930 [cLyo32] brought completely

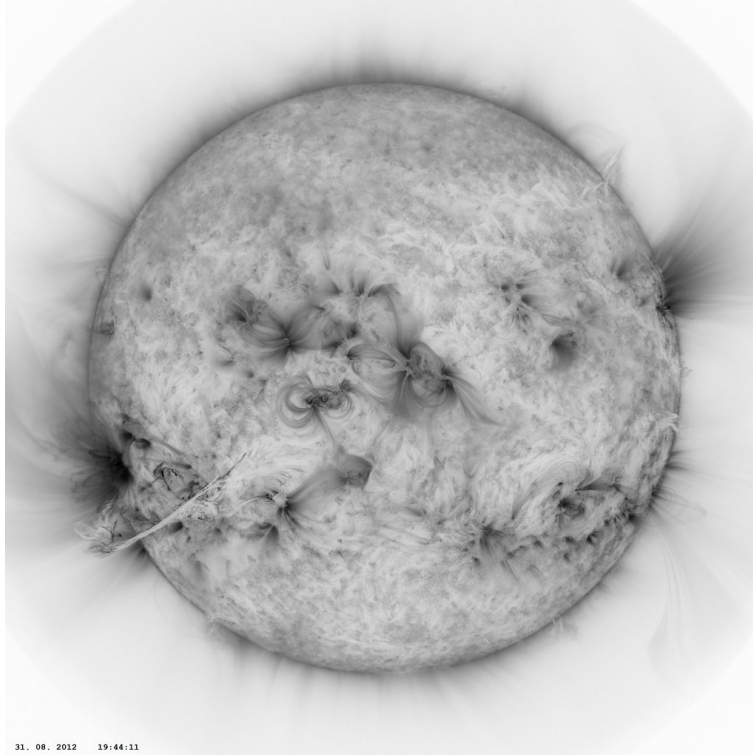


Figure 2.1: An image of the inner corona as observed by the Atmospheric Imaging Assembly, which is part of the Solar Dynamics Observatory (NASA) in the ultraviolet part of the spectrum – 171 Å. Image downloaded from [dVso13], in negative.

new possibilities by enabling daily observations of the inner corona in visible light and in specific spectral lines as well as in polarized emission. Current cosmic probes such as SOHO LASCO [cBHK95] use coronagraphs. However, due to diffraction on the edge of the occulter, the innermost part of up to 1.05 solar radii ( $1.05 R_{\odot}$ ) the corona still remains unobservable with coronagraphs.

A possibility to observe the innermost corona is imaging in the ultraviolet, extra-ultraviolet (EUV) and X-ray wavelength ranges, where the photosphere is completely black. This has to be done from outside the Earth's atmosphere, which filters out these wavelengths. However, spectral lines of heavy ions in these wavelength ranges are only collisionally excited and cannot be observed as far away from the Sun as emission from Fe X 637.4 nm e.g., that has a radiative component and significantly longer wavelength.

Even though there are sophisticated methods for continuous observations of the solar corona, the rare occasions of total solar eclipses are still the only times when the innermost corona can be observed in the visible part of the spectrum with orders of magnitude cheaper equipment than spaceborne observatories and with high resolution.

## 2.3 Methods of compensation for the brightness gradient

**Remark 2.1.** The term radial gradient is commonly used among solar astronomers. It means that the brightness gradient of the image is a vector whose direction is approximately radial, i.e. there is a high directional derivative of the image in the radial direction.

The mechanical and optical methods of compensation for the brightness gradient are treated in the full version of the doctoral thesis. Here, we stick to the mathematical methods – methods of digital image processing.

Since the 1980s, the increasing power of computers enabled software implementation of mathematical image-processing techniques. They have become more and more complicated with more powerful computers. Apart from classical high-pass filters with relatively small kernels of  $3 \times 3$  or  $5 \times 5$  pixels, which brought about significant noise enhancement, other methods of digital image processing were proposed, e.g. the MaD Max II method introduced by Olga Koutchmy and her colleagues [cKKN88].

In late 1990s, the increasing power of computers made possible the use of larger kernels for filters and went together with the development of image processing software for common users. In 2000 Fred Espenak described a powerful technique for visualization of coronal structures in digitized images which uses a common image-processing software – Adobe Photoshop [cEsp00]. This technique (described in the full version of the doctoral thesis in Section 5.1) and its variations have been commonly used since that time.

The method proposed and implemented by myself and by my father Miloslav Druckmüller [bDru03, aDru05, cDRM06] in the Corona software gives results that are closer to human vision during the total solar eclipse (TSE), because they use multiple two-dimensional direction-invariant kernels with different sizes. This method, which is later referred to as the Adaptive Circular High-pass Filter (ACHF) is described in Section 5.2 in the doctoral thesis.

The Normalizing-radial-graded-filter (NRGF) was published by Huw Morgan and his colleagues in 2006 [cMHW06]. It is completely automated, therefore it has been used as a standard tool for processing images from coronagraphs.

During my Ph.D. study I proposed and implemented the Fourier normalizing-radial-graded filter (FNRRGF), which was first published in [aDMH11] and is the core of my doctoral thesis. It is inspired by the NRGF. The FNRRGF is described in Chapter 3.

# 3 Fourier normalizing-radial-graded filter

This chapter contains the main contribution of the doctoral thesis - the newly developed Fourier normalizing-radial-graded filter (FNRGF). The filter is inspired by the Normalizing-radial-graded filter.

## 3.1 Normalizing-radial-graded filter

The normalizing-radial-graded filter [cMHW06] solves the problem of the steep radial gradient of image brightness and structure contrast by segmenting the corona into narrow circular regions centered on the center of the Sun, and by calculating an average and standard deviation of brightness for each region. Each pixel is processed according to its height (distance from the photosphere) within the image by subtracting the average (thus removing the steep radial gradient) and dividing by the standard deviation (thus removing the radially decreasing brightness contrast) of values of all pixels in the region.

In this chapter, we will assume that we have an image showing the solar corona off the edge of the solar disk with linear dependence of pixel value on coronal brightness which is a result of the sequence of steps starting from image acquisition including image calibration, registration and composition in one high-dynamic-range image. This image will be called the original image  $f$  and will be indexed both in Cartesian coordinates  $[x, y]$  and heliocentric polar coordinates  $[r, \varphi]$ .

The resulting image  $g$  is computed as (using the notation from [cLiM83])

$$g(r, \varphi) = \frac{f(r, \varphi) - \overline{f(\rho, \varphi)|_{\rho=r}}}{S(f(\rho, \varphi)|_{\rho=r})} = \frac{f(r, \varphi) - E(r)}{\sqrt{\frac{1}{N_r-1} \sum_{\rho=r} (f(\rho, \varphi) - E(r))^2}}, \quad (3.1)$$

$$\text{with } E(r) = \frac{1}{N_r} \sum_{\rho=r} f(\rho, \varphi),$$

where  $N_r$  denotes the number of pixels in the image that have the rounded distance from the center of the Sun in the image equal to  $r$ . Formula (3.1) is applied only to circles in the image that lie completely in the corona. An example of an image processed with the NRGF is in Figure 3.8 on page 24.

## 3.2 The principle of the filter

The NRGF approach applies the same transformation to all pixels in each circle. Therefore, it cannot compensate for a different contrast of structures at the same height. However, there might be both sections with relatively low contrast and fine structures and relatively high contrast and prominent structures on one circle. This is typical for the solar corona in the minimum of the solar cycle, where the polar regions are quiet (darker and with lower contrast) and the active regions with higher brightness and contrast are in a belt of latitudes around the equator (most images of the corona here are from the minimum to the rising phase of solar activity in years 2006 to 2010). The NRGF does not visualize these fine structures, because their contrast is too low compared to the rest of the circle. The aim of the FNRGF, which was proposed as part of my Ph.D. study, is to eliminate this drawback, i.e. to propose a filter which is inspired by the NRGF (normalizing by subtracting the average and dividing by the standard deviation) but offering higher adaptivity. The proposed filter with its principle, with all parameters involved, and the results are described in this chapter. The FNRGF was implemented in the FNRGF software (see Section 3.4).

The idea of the filter is as follows: instead of subtracting one number from all values of pixels on one circle and then dividing all of them by the same number, these numbers are computed adaptively, being different for different position angles on one circle. The basic principle of the filter is described in Section 3.2.1. The filter uses trigonometric polynomials to estimate the local averages and local standard deviations of pixel values. However, it turned out that the trigonometric polynomials had to be modified – attenuated with increasing order of the Fourier coefficients. The attenuation coefficients used for this purpose, their function and their settings are treated in Section 3.2.2. The noise contained in the processed images has an impact on the filter, which can be compensated for as is discussed in Section 3.2.3.

### 3.2.1 The basic idea of the filter

The steps of the computation of the filter are enumerated below, the same numbering is kept for expressing the process in formulae, as described below in this section.

- (1) **Which pixels are processed?** Only pixels on Sun-centered circles that lie completely in the corona are processed (not partially obscured by the Moon, not partially out of the image). Let us denote this set of pixels by  $M_{\odot}$ .

- (2) **Angular and radial segments.** The content of  $M_{\odot}$  is split into one-pixel thick Sun-centered circles and those in tens of non-overlapping angular segments ( $n_s$  is the number of segments). Different segments contain generally a different number of pixels, because the number of pixels in each segment increases with height  $r$  and also the circles are discrete, which means that pixels are not spread evenly in segments on one circle. Figure 3.1a is an illustration of an image being split into segments.
- (3) **Averages, standard deviations, Fourier approximations.** Two quantities are calculated in each segment – the average pixel value and the standard deviation of pixel values. Thus we obtain two functions of two discrete variables, each of them a function of height  $r$  and segment index  $s$ . These functions are then approximated with a trigonometric polynomial of order  $\omega$ . Approximation by the trigonometric polynomial was selected due to its  $2\pi$ -periodicity. Figure 3.1b gives an idea of this approximation (the attenuation coefficients mentioned there will be described below).

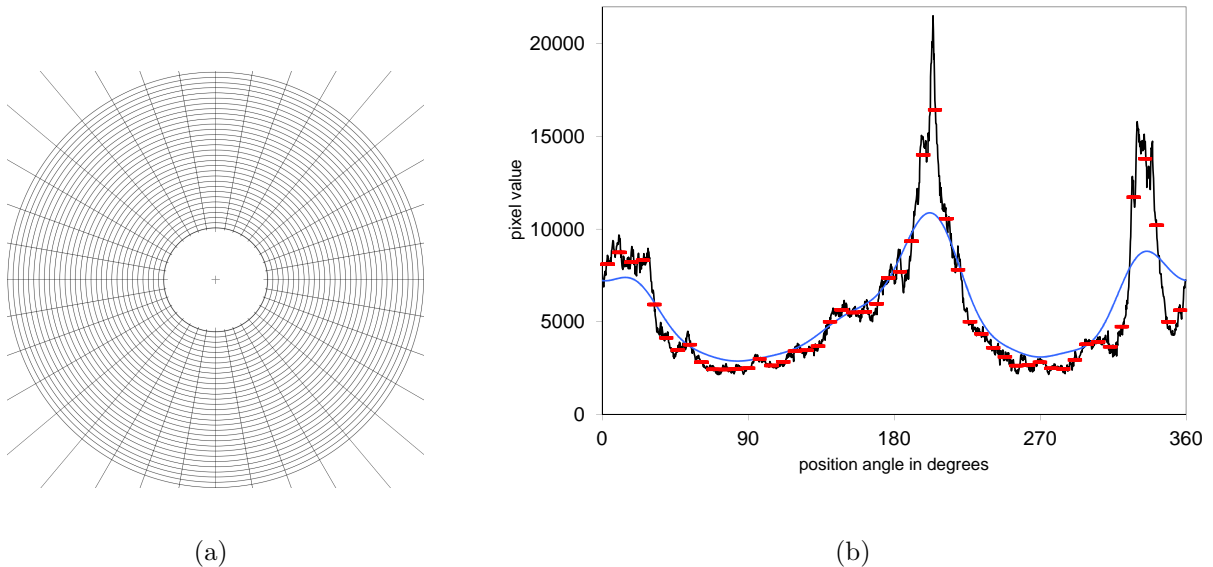


Figure 3.1: Illustration of the computation of the FNRGF. Figure (a) shows an image being split in circles and angular segments. The figure is simplified in the sense that in practice the annuli are only one pixel wide and there are more angular segments. Figure (b) documents the computation. The black line represents original image values, the red bars represent the averages in each of the 50 segments, and the blue line is a Fourier approximation of these averages with a trigonometric polynomial of order  $\omega = 10$  with attenuation coefficients set to  $A_0 = 1$ ,  $A_1 = 0.9$ ,  $A_2 = 0.8$ ,  $\dots$ ,  $A_{10} = 0$ . The attenuation coefficients are discussed in Section 3.2.2. Figure prepared for [aDMH11].

- (4) **Normalization.** Now, the concept of the NRGF is used and further developed. Each pixel in the image is processed by subtracting the Fourier approximation of the average and dividing by the Fourier approximation of the standard deviation, at the particular height  $r$  and position angle  $\varphi$  of that pixel.
- (5) **Combination with the original image.** Finally, the image filtered with the algorithm described above is combined with the original image to keep some information (feeling) about the absolute brightness of the corona in the image. Pixels that lie out of  $M_\odot$  are not processed, they are left black in the resulting image.

The steps above are described more precisely and in steps and in the formulae that follow.

- (1) The set  $M_\odot$  is the set of all pixels  $[r, \varphi]$  in the image with  $r_o \leq r \leq r_c$ , where  $r_o$  is the radius in pixels of the smallest circle that lies completely in the corona and  $r_c = \min\{o_x, o_y, w - 1 - o_x, h - 1 - o_y\}$  is the radius of the largest circle that has its center in the center of the Sun in the image and lies completely in the image. ( $O = [o_x, o_y]$  is the center of the Sun in the image,  $w$  is the image width,  $h$  the image height.)
- (2) The content of  $M_\odot$  is split into segments.  $s = 0, 1, \dots, n_s - 1$  are indices of the segments, which are evenly spread on each circle, therefore pixels with  $\varphi \in \left\langle \frac{2\pi}{n_s}s, \frac{2\pi}{n_s}(s+1) \right\rangle$  belong to the  $s$ th segment. The number of segments  $n_s$  must be at least as high as the number of Fourier coefficients involved in the filter, which is  $2\omega + 1$ . Furthermore, the number of segments must be several times lower (it is advised to be ten times) than the circumference of the smallest circle in the image that lies completely in the corona ( $2\pi r_o$ ) so that the standard deviations of pixel values in the segments are trustworthy numbers. In the radial direction, the segments are indexed with their height  $r$  in pixels.
- (3) In this step, the average values and the standard deviations of pixel values in each segment are computed. Let us denote the average of values in segment  $s$  at height  $r$  by  $E_s(r)$ . With the notation inspired by [cLiM83], it can be written as

$$E_s(r) = \overline{f(\rho, \varphi)}_{\rho=r, \varphi \in \left\langle \frac{2\pi}{n_s}s, \frac{2\pi}{n_s}(s+1) \right\rangle} = \frac{1}{N_{r,s}} \sum_{\substack{\rho=r \\ \varphi \in \left\langle \frac{2\pi}{n_s}s, \frac{2\pi}{n_s}(s+1) \right\rangle}} f(\rho, \varphi),$$

where  $N_{r,s}$  is the number of pixels in the image whose rounded distance from the center of the Sun is equal to  $r$  and which belong to the  $s$ th segment, the initial version of the filter could be described by the following formulae:

$$a_{r,0} = \frac{2}{n_s} \sum_{s=0}^{n_s-1} E_s(r) \quad (3.2)$$

$$a_{r,k} = \frac{2}{n_s} \sum_{s=0}^{n_s-1} E_s(r) \cos \frac{2\pi k(s + \frac{1}{2})}{n_s}, \quad k = 1, 2, \dots, \omega \quad (3.3)$$

$$b_{r,k} = \frac{2}{n_s} \sum_{s=0}^{n_s-1} E_s(r) \sin \frac{2\pi k(s + \frac{1}{2})}{n_s}, \quad k = 1, 2, \dots, \omega \quad (3.4)$$

Coefficients  $a_{r,0}, a_{r,1}, \dots, a_{r,\omega}, b_{r,1}, \dots, b_{r,\omega}$  are coefficients of the trigonometric polynomial of the function given by values of the average pixel value in each segment at each height  $r$ . Integrals which would be necessary for the analytical computation of these coefficients are computed numerically by means of the rectangular rule. Coefficients  $c_{r,0}, c_{r,1}, \dots, c_{r,\omega}, d_{r,1}, \dots, d_{r,\omega}$  for the standard deviation are computed in analogy with those for the averages [cLiM83].

$$\begin{aligned} S_s^2(r) &= S^2 \left( f(\rho, \varphi) \Big|_{\rho=r, \varphi \in \langle \frac{2\pi}{n_s}s, \frac{2\pi}{n_s}(s+1) \rangle} \right) = \\ &= \frac{1}{N_{r,s} - 1} \sum_{\substack{\rho=r \\ \varphi \in \langle \frac{2\pi}{n_s}s, \frac{2\pi}{n_s}(s+1) \rangle}} (f(\rho, \varphi) - E_s(r))^2 \end{aligned} \quad (3.5)$$

$$c_{r,0} = \frac{2}{n_s} \sum_{s=0}^{n_s-1} \sqrt{S_s^2(r)} \quad (3.6)$$

$$c_{r,k} = \frac{2}{n_s} \sum_{s=0}^{n_s-1} \sqrt{S_s^2(r)} \cos \frac{2\pi k(s + \frac{1}{2})}{n_s}, \quad k = 1, 2, \dots, \omega \quad (3.7)$$

$$d_{r,k} = \frac{2}{n_s} \sum_{s=0}^{n_s-1} \sqrt{S_s^2(r)} \sin \frac{2\pi k(s + \frac{1}{2})}{n_s}, \quad k = 1, 2, \dots, \omega. \quad (3.8)$$

The Fourier approximations of the mean and the standard deviation

in each pixel are computed as

$$F_{\bar{f}}(r, \varphi) = \frac{a_{r,0}}{2} + \sum_{k=1}^{\omega} (a_{r,k} \cos k\varphi + b_{r,k} \sin k\varphi) \quad (3.9)$$

$$F_{S(f)}(r, \varphi) = \frac{c_{r,0}}{2} + \sum_{k=1}^{\omega} (c_{r,k} \cos k\varphi + d_{r,k} \sin k\varphi). \quad (3.10)$$

Note that the sines and cosines in the formulae for  $a_{r,0}$ ,  $a_{r,k}$ ,  $b_{r,k}$ ,  $c_{r,0}$ ,  $c_{r,k}$ ,  $d_{r,k}$  (Equations (3.2)–(3.4) and (3.6)–(3.8)) and the sines and cosines in the Fourier approximations (Equations (3.9) and (3.10)) have different arguments. This is correct, because the former refer to values in  $n_s$  segments, the values are known only in tens of evenly spread points, whereas the latter refer to angles in the interval  $\langle 0, 2\pi \rangle$ .

(4) The filtered image  $g$  is computed as

$$g(r, \varphi) = \begin{cases} \frac{f(r, \varphi) - F_{\bar{f}}(r, \varphi)}{F_{S(f)}(r, \varphi)} & \text{if } [r, \varphi] \in M_{\odot} \\ 0 & \text{else.} \end{cases}$$

The formula involves division, but there is no need to treat division by zero. Standard deviations of pixel values in a real image (with noise) are always strictly positive and their Fourier approximations as well (the Fourier approximation cannot be lower than the lowest value in the sequence). Note that setting the number of angular segments  $n_s = 1$  (which means that  $\omega = 0$ ) converts the FNRGF into the NRGF.

(5) To preserve some information about the absolute brightness of image  $f$ , the filtered image  $g$  is then linearly combined with the original image to create image

$$h(x, y) = \begin{cases} h(x, y) = K_1 \cdot f(x, y) + K_2 \cdot g(x, y) & \text{if } [x, y] \in M_{\odot} \\ 0 & \text{else,} \end{cases}$$

where  $K_1, K_2 > 0$ .

### 3.2.2 Attenuation coefficients

When the above described filter was implemented, it turned out that a trigonometric polynomial can approximate the pixel values and the local contrast of the original image too well. The filtered image contained only

structures of a particular size (not the most prominent, but also not the finest as e.g. from the ACHF – depending on the order of the trigonometric polynomial  $\omega$ ) and then some deviant pixel values caused by stars or impulse noise, therefore the contrast of the visualized structures was very low. The necessity to treat information on different spatial frequencies in a different manner was inevitable.

This is the reason why I introduced the *attenuation coefficients* – Equations (3.9) and (3.10) were changed to

$$F_{\bar{f}}(r, \varphi) = A_0 \frac{a_0}{2} + \sum_{k=1}^{\omega} A_k (a_{r,k} \cos k\varphi + b_{r,k} \sin k\varphi)$$

$$F_{S(f)}(r, \varphi) = C_0 \frac{c_0}{2} + \sum_{k=1}^{\omega} C_k (c_{r,k} \cos k\varphi + d_{r,k} \sin k\varphi),$$

with attenuation coefficients  $A_0, \dots, A_{\omega}, C_0, \dots, C_{\omega} \in \langle 0, 1 \rangle$ . The series of  $A_k$  and the series of  $C_k$  should be non-increasing so that the filter treats information on different spatial frequencies in a monotonous way. There are  $2\omega$  attenuation coefficients in total, involved in the filter.

### Correct values of attenuation coefficients

The proper setting of the attenuation coefficients depends on the size of the image, on its quality (signal : noise ratio) and the distribution of structures in the image. At present, these parameters have to be set manually, the FNRGF software only contains a tools for setting more coefficient values together. Examples of suitable settings of the attenuation coefficients can be found in Section 3.3.1.

An illustration of an incorrect (too high) setting of the coefficients can be found in Figure 3.2. If the  $A_k$ s are set too high (Figure (a)), it causes artificial brightenings in the low-contrast parts of the image. They are false glimmers of the higher-order sine and cosine functions. These may not appear in every image, as they depend on the distribution of the structures in the image. Another indicator that the  $A_k$ s are set too high is that we are losing contrast in the image, especially at lower spatial frequencies. We are enhancing only the finest details that can be visualized with the FNRGF with one setting of  $\omega$ , not the full range of structure sizes. Setting  $C_k$  too high (Figure (c)) may have destructive effects on the image. Some structures become strongly enhanced and if the coefficients are enhanced even more, these artifacts will dominate the whole dynamic range of the image.

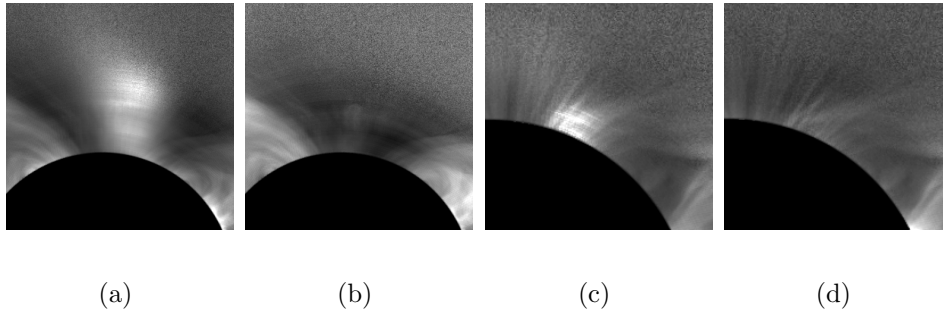


Figure 3.2: Illustration of proper and improper setting of attenuation coefficients, using the 2010 total solar eclipse observations of Fe XIV emission ((a), (b)) and Fe X emission ((c), (d)). The attenuation coefficients for the average are too high in Figure (a), but are close to optimal in (c). Similarly, the parameters for the standard deviation are too high in Figure (b) and are close to optimal in (d). Figure prepared for [aDMH11]

On the other hand, too low values of the coefficients are not as fatal as too high values provided they are low for both  $A_k, C_k$ . They only do not make use of the full advantage of the FNRGF, i.e. the structures are not visualized as much as they could. If the coefficients are around the optimum, a slight increase of  $A_k$  decreases the local contrast, whereas a slight increase of  $C_k$  increases the local contrast (including noise). The optimal setting of the coefficients seems to have  $A_k$  decreasing more slowly than  $C_k$ .

### Fourier-analysis explanation for attenuation coefficients

The sense of attenuation coefficients can also be described in terms of the Fourier analysis. The Fourier coefficients  $a_{r,k}, b_{r,k}, c_{r,k}, d_{r,k}$  contain information on different spatial frequencies. The setting of attenuation coefficients attenuates information on the corresponding frequencies – they form a low-pass filter for the unsharp mask, which is used in the high-pass filter. In fact, the FNRGF cannot be simply expressed as subtracting an unsharp mask, but we can intuitively use the idea. This can be, in principle, always done in two ways – by multiplication in the frequency domain and by convolution in the spatial domain. Here I chose the first option due to the use of the trigonometric polynomials. Expressing the attenuation by means of convolution can be a tricky task once it is done in the frequency domain. Computing the Fourier transform analytically is in general non-trivial. However, what is necessary is for the filtration to be monotone with respect to frequencies, i.e. the sequence of attenuation coefficients must be non-increasing.

### 3.2.3 Influence of additive noise

Every image produced from frames acquired with a camera (i.e. not computer graphics) contains additive noise, its amount depends on the temperature, lighting of the scene, on the camera sensor and in the case of images composed from more images also on the number of images used. If the image is composed from images with different exposure settings, the amount of noise in different parts of the image is different. In TSE images of the solar corona, most of the noise comes from the noise in the eclipse images, much less from calibration images, because it is possible to take many calibration images after totality to reduce the noise in the calibration data.

The noise in the image increases the standard deviation of pixel values that is computed as part of the FNRGF computation. Each image  $f$  can be written as a sum of an ideal noiseless image  $i$  and the noise  $n$ ,  $f(x, y) = i(x, y) + n(x, y)$ . If we consider  $i$  and  $n$  as two random variables, the mean of  $f$  is  $\mathbb{E}f = \mathbb{E}i + \mathbb{E}n$  (both for the whole image and locally). If the noise has normal distribution with zero mean (a standard assumption), the mean of  $f$  equals to the mean of  $i$  and we can conclude that the mean of  $f$  is not affected by the noise (in the ideal, asymptotic case).

If we further assume that  $i$  and  $n$  are independent, the variance of  $f$  is the sum of variances of  $i$  and  $n$ ,  $\mathbb{D}f = \mathbb{D}i + \mathbb{D}n$ . The presence of additive noise with a constant variance throughout the image causes a constant increase of the local variance used in the FNRGF. Since the FNRGF divides by the local standard deviation, the division by a higher number causes lower enhancement in the whole image. However, removing the effect of additive noise by subtracting its variance before using the local standard deviation in the FNRGF (as published in [aDMH11]) is a misleading idea. If there is a part in the image that contains only noise, this idea of dividing by the local  $\sqrt{\mathbb{D}i}$  instead of  $\sqrt{\mathbb{D}f}$  leads to infinite amplification in this part of the image (infinite amplification of noise).

The solution that is implemented in the FNRGF software is inspired by the method used in the NAFE [cDru13]. The problem is that extreme amplification in low-contrast areas leads to loss of details in these parts of the image (because they will be dominated by noise). In extreme cases the amplified noise has higher contrast than the prominent structures in the inner corona causing the additive noise to set the range of the image pixel values and decrease the contrast of these prominent structures in the filtered image.

The solution is exactly the opposite – adding noise instead of subtracting it. Artificial noise that is independent from the image and the image

noise, added to the original image adds a constant to the local variances throughout the image and decreases the relative contrast of the original noise. In parts of the image which are dominated by noise, this decreases the amplification, i.e. decreases the influence of the noise. The noise that is added has a negligible effect in parts of the image with prominent structures since the structures lead to high local variances. If the noise is added in the image, we need a random generator and a new image matrix in the computer memory to keep both the original image and the image with artificially added noise. A more efficient solution is to add the variance of the artificial noise to the local variances only in the computation of the FNRGF, i.e. Equations (3.6) - (3.8) are changed to

$$c_{r,0} = \frac{2}{n_s} \sum_{s=0}^{n_s-1} \sqrt{S_s^2(r) + V_n}$$

$$c_{r,k} = \frac{2}{n_s} \sum_{s=0}^{n_s-1} \sqrt{S_s^2(r) + V_n} \cos \frac{2\pi k(s + \frac{1}{2})}{n_s}, \quad k = 1, 2, \dots, \omega$$

$$d_{r,k} = \frac{2}{n_s} \sum_{s=0}^{n_s-1} \sqrt{S_s^2(r) + V_n} \sin \frac{2\pi k(s + \frac{1}{2})}{n_s}, \quad k = 1, 2, \dots, \omega,$$

where  $V_n$  is the variance of the artificial noise. Decreasing the relative contrast of the original noise and its amplification allows a bigger part of the dynamic range of the filtered image for the contrast of the coronal details thus allowing higher attenuation coefficients and higher enhancement of coronal structures.

The FNRGF software allows the user to set  $\sqrt{V_n}$  – the standard deviation of the artificial noise. Experiments with images taken in spectral lines of Fe ions during the 2010 TSE show that the optimal values of  $\sqrt{V_n}$  are about 10 to 15 percent of the standard deviation of the noise originally contained in the image. This standard deviation is estimated as the median of standard deviations in all radial and angular segments that are close to the outer edge of the processed corona. Pixels in the 10 outermost rings are taken into account. The number of 10 to 15 percent is in accordance with a test made with the NAFE [cDru13] on SDO AIA data. Figure 3.3 illustrates the effect of  $V_n$  on the filtered image. The decreasing amount of noise in the filtered image with increasing  $V_n$  is clearly visible. Other parameters are identical for all three images.

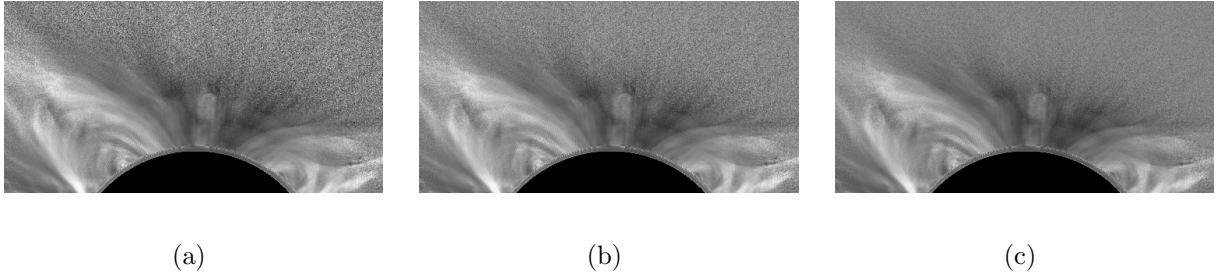


Figure 3.3: Illustration of the effect of artificially added noise in the FNRGF on a section of the Fe XIV image taken during the 2010 TSE.  $\sqrt{V_n}$  was set to 0 (a), 7.5% of the noise in the original image estimated from 2.618 to 2.68  $R_\odot$  (b), and 15% of the noise in the original image (c). The attenuation coefficients  $A_k$  were linearly decreasing with a step of 0.03,  $C_k$  with a step of 0.04. The filtered image was mixed with the original image in the ratio of 7 : 1 after being both of them normalized to  $\langle 0, 1 \rangle$ .

## 3.3 Results

### 3.3.1 Application to total solar eclipse observations

The FNRGF was originally designed for images from spectral line emission taken during total solar eclipses, which were also its first testing data. Figure 3.4 is a complete collection of images of emission of heavy ions as observed by the team of prof. Habbal during the 2010 TSE. The images were processed with the latest version of the FNRGF software with the highest possible number of segments  $n_s$  and the highest possible order of the trigonometric polynomial  $\omega$ , for most of the images,  $n_s$  was set to 100 (101 was the highest possible if we estimate the number of pixels in each of the segments in the smallest circle in the corona to 10 by setting  $n_s$  equal to one tenth of the circumference of this circle). For these images, the attenuation coefficients  $A_k$  were set to  $(1, 0.97, 0.94, \dots)$ , the coefficients  $C_k$  were  $(1, 0.96, 0.92, \dots)$ . The images were processed up to a height of 2.5  $R_\odot$ . The only two images that were processed up to the height of only 2  $R_\odot$  are Fe IX and Ni XV (Figures (a) and (f)), which also had a lower number of segments (50) and their trigonometric polynomials were attenuated more ( $A_k$ s set to  $(1, 0.95, 0.90, \dots)$ ,  $C_k$ s to  $(1, 0.94, 0.88, \dots)$ ). These images have lower signal to noise ratio, the Ni XV line is relatively weak. In the case of Fe XIII it is caused by the low quantum efficiency of the camera at this wavelength, only approximately 1.5 percent. That is why the structures in these images cannot be enhanced as much as in the other images.

At present, these are the best images showing the fine structure of the corona in emission from coronal forbidden lines from heavy ions. The high quality of the data, the high adaptivity of the FNRGF due to higher

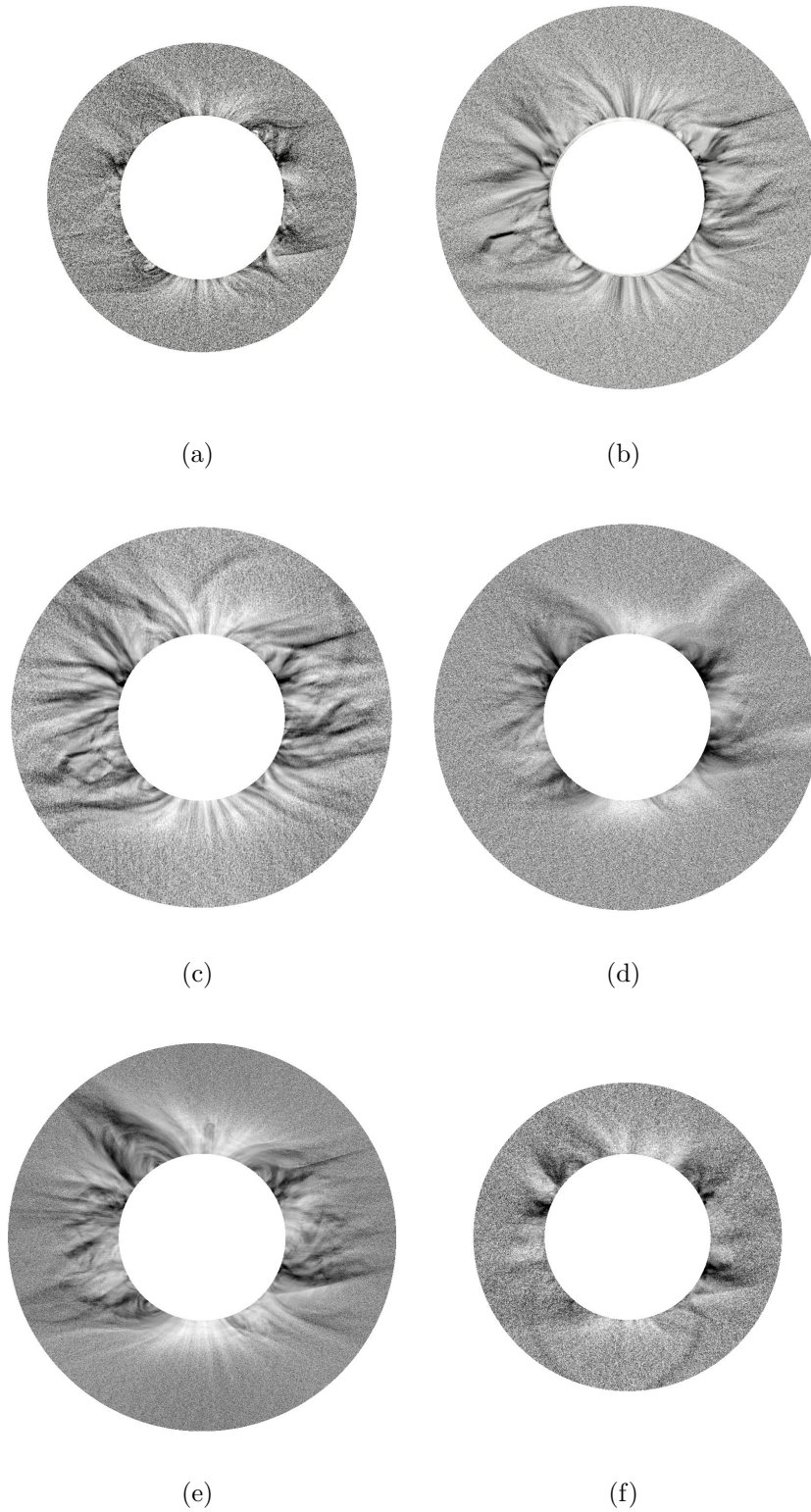


Figure 3.4: A complete set of images of radiation from heavy ions observed during the 2010 TSE [aHDM11] and processed with the FNRGF. (a) Fe IX 435.9 nm, (b) Fe X 637.4 nm, (c) Fe XI 789.2 nm, (d) Fe XIII 1074.7 nm, (e) Fe XIV 530.3 nm, (f) Ni XV 670.2 nm. All images are shown as negatives. To compare the results with processing with the NRGF and ACHF see [aHDM11].

order terms and the separate processing of each circle enables the filter to compensate for the enormous brightness gradient and visualize structures further from the Sun.

For application of the FNRGF to a white-light image from a total solar eclipse see page 26 – Comparison with the ACHF in Section 3.3.3.

### 3.3.2 Application to space-based observations

The FNRGF is of course not limited to eclipse images. I show here how the application of this tool significantly improves the depiction of coronal structures in coronagraph and extreme ultraviolet (EUV) images.

Figure 3.5 shows the application of the FNRGF to an EUV observation from the EUV Imaging Telescope (EIT) aboard the Solar and Heliospheric Observatory (SOHO), which observes the chromosphere and low corona in collisionally excited emission lines of highly ionized iron. The 195 Å bandpass is dominated by Fe XII at a formation temperature of around 1.5 MK, and in Figure 3.5 I present an image taken in this bandpass about five minutes after the eclipse observations of the team of prof. Habbal during the 2010 TSE. The outer part of the image was processed by means of FNRGF to enhance details in the solar corona. Before applying the filter, impulse noise (for example, faulty pixels, or hits of the sensor by high-energy particles) was filtered out from the original image by means of a one-pass median filter. The image reveals fine-scale structures in the innermost corona, as well as their connections to structures on the solar disk, which were completely invisible in the original image.

Figure 3.6 shows the application of the FNRGF to an observation by the Large Angle and Spectrometric Coronagraph (LASCO) C2 coronagraph near to the time of the eclipse observations of the team of prof. Habbal during the 2010 TSE. A significant amount of impulse noise was filtered from the image by means of a one-pass median filter before application of the FNRGF and still some impulse noise is visible in the images. Since the FNRGF subtracts the local average of brightness, it enhances structures in the darker polar regions, thus revealing polar plumes at all heights within the field of view. These would otherwise remain invisible - even with the NRGF processing, which basically enhances the structures with the highest contrast at a given height. Other interesting structural details are revealed in the equatorial streamer region.

Among successful application of the FNRGF is the visualization of the comet C/2011 W3 (Lovejoy) in 171 Å images acquired by the Atmospheric Imaging Assembly aboard the Solar Dynamic Observatory (SDO AIA) shortly after the comet reached perihelion (Figure 3.7). None of the previously used filters were able to visualize the comet and the surrounding

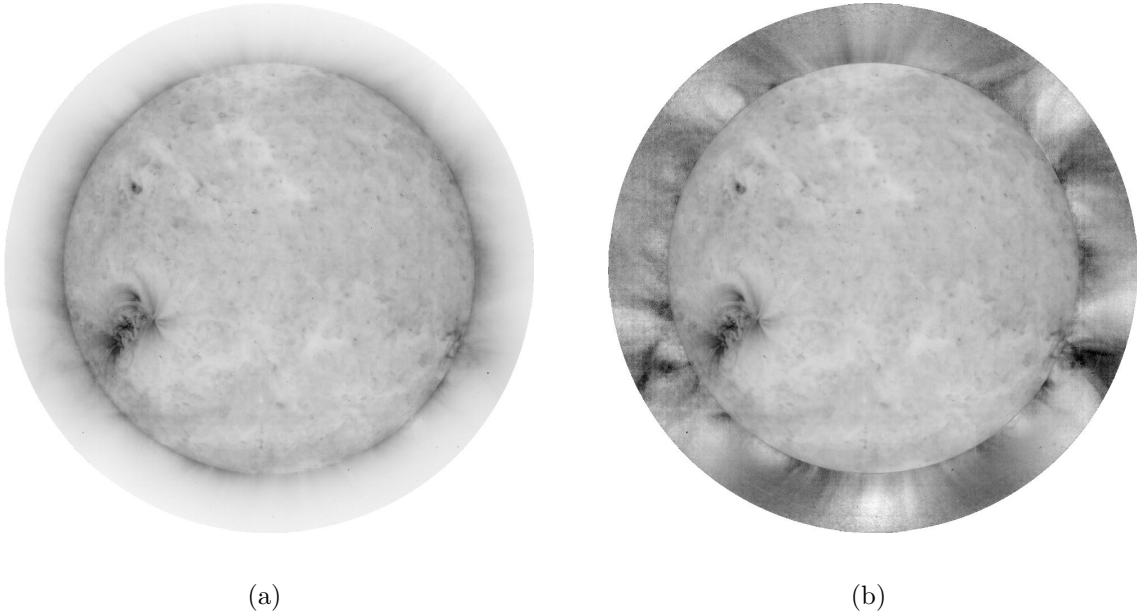


Figure 3.5: (a) A SOHO EIT (Extreme Ultraviolet Imaging Telescope aboard the Solar and Heliospheric Observatory) 195 Å observation taken near to the time of the total solar eclipse observation by the IfA UH team on July 11, 2010. The off-limb field of view is cropped to  $1.3 R_{\odot}$ . (b) The same image with off-limb regions processed by the FNRGF to enhance structural details. The solar disk is taken from the original image. Figure prepared for [aDMH11], in negative.

corona in a similar way to show the tail of the comet enhancing emission along the magnetic field lines intercepted by the passage of the comet. The high adaptivity of a high-order FNRGF allowed the fine details to be visualized. These results are being prepared for publication.

### 3.3.3 Comparison with other methods

#### Comparison with the NRGF

The predecessor of the FNRGF, the NRGF was described in Section 3.1. Compared to the NRGF, the FNRGF gives much more detailed images, visualizes finer structures. On the other hand, it is computationally slower and requires user setting of parameters. The NRGF is automatic and fast.

The FNRGF software enables the user to process images with the NRGF, even though it is an overkill. It requires setting  $n_s = 1, \omega = 1, A_0 = C_0 = 1, A_1 = C_1 = 0$ . The mathematically logical solution would be  $\omega = 0$ , but the FNRGF software is designed in a way that it needs the trigonometric polynomial of at least order 1 (there is a for cycle for  $k$  from 1 to  $\omega$ ).

Figure 3.8 compares the application of the NRGF and the FNRGF to the Fe XIV 530.3 nm observation of the team of prof. Habbal of the Institute

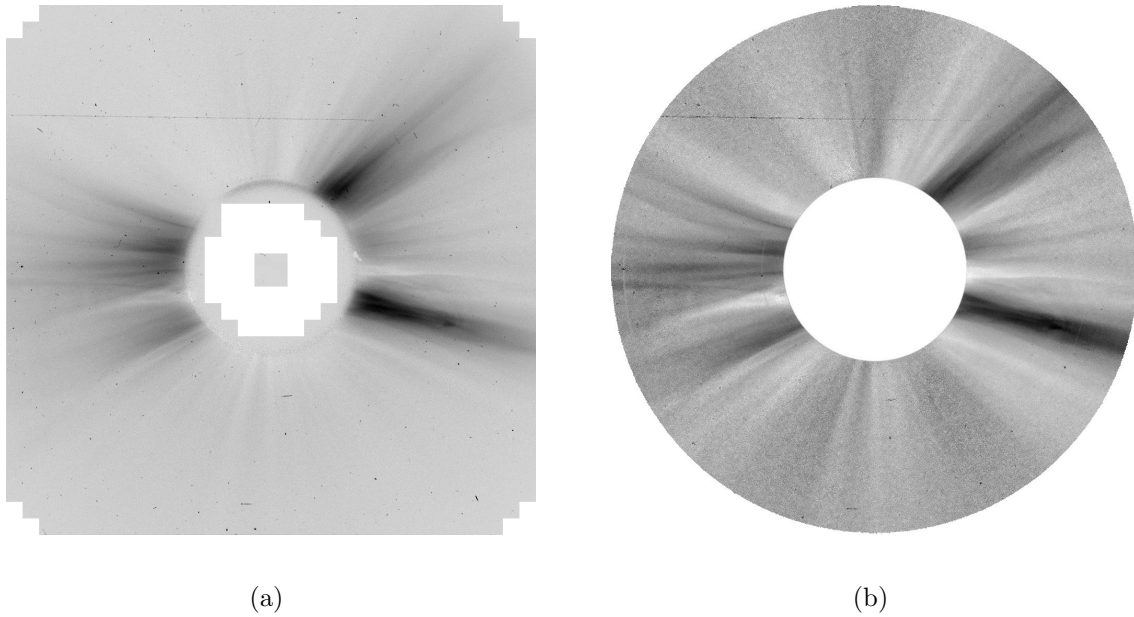


Figure 3.6: a) A LASCO/C2 white light brightness observation taken near to the time of the total solar eclipse on July 11, 2010. The inner limit of the field of view is  $\sim 2.2 R_{\odot}$ , as dictated by the occulting disk. The outer field of view extends to  $\sim 6 R_{\odot}$  at the center of the image edges. (b) The same image processed by the FNRGF to enhance structural details. Regions outside the annulus which were processed are set to white (black in the processed image). Figure prepared for [aDMH11], in negative.

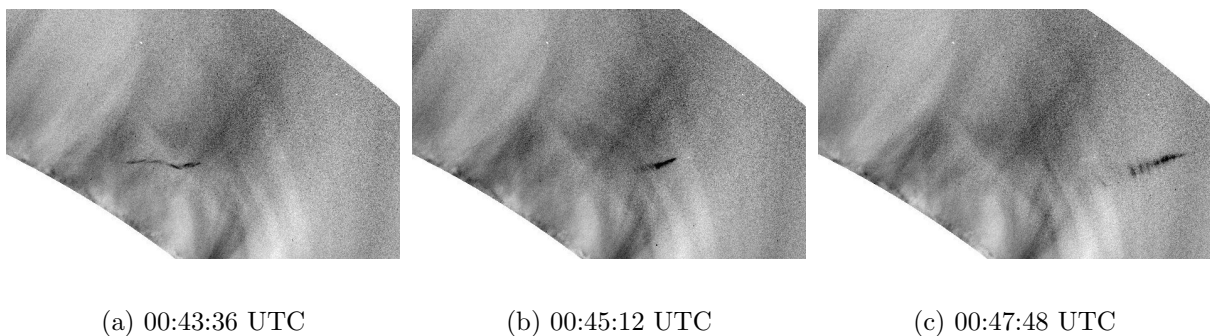


Figure 3.7: A series of images of comet C/2011 W3 (Lovejoy) shortly after it reached perihelion on 2011-12-16 in  $171 \text{ \AA}$  images as observed by the SDO AIA. The whole images were processed with the FNRGF, but only small sections are shown here as negatives. The original images were downloaded from [dVso13], in negative.

for Astronomy, University of Hawaii during the 2010 TSE. Figure (a) shows the application of the NRGF, Figure (b) the FNRGF.

### Comparison with the ACHF

The Adaptive circular high-pass filter (ACHF) is given in the full version of the thesis and in articles [bDru03, aDru05, cDRM06]. It has a completely different principle from the FNRGF as it is based on adaptive convolution

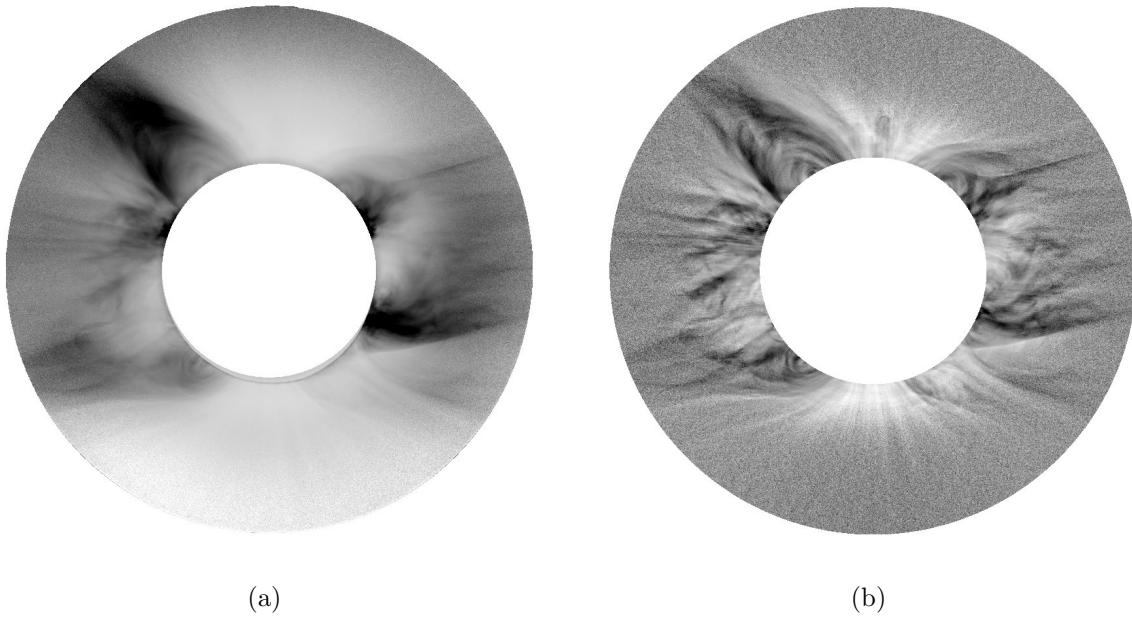


Figure 3.8: The same original image processed by NRGF (a) and FNRGF (b). The original image is an image of Fe XIV emission as observed by the team of prof. Habbal during the 2010 TSE. Figure (a) prepared for [aDMH11], in negative.

with several kernels. What can be compared based on the principle of the filters is the size of the enhanced structures. Both filters have a technique to control the size of the enhanced structures. In the ACHF, it is the parameters of the Gaussian functions used for the kernels, in the FNRGF, it is the order of the trigonometric polynomial and the attenuation coefficients. An important advantage of the ACHF compared to the FNRGF is that it can process the whole image, the FNRGF can only process pixels in  $M_{\odot}$  (defined in step (1) on page 12).

A comparison of an image processed with the ACHF and the FNRGF is given in Figure 3.9. Even with the highest possible setting of the order of the trigonometric polynomial, the FNRGF cannot enhance as fine details as the ACHF. The advantage of the FNRGF compared to the ACHF is visualization of details in the corona at higher heights. As the FNRGF processes each circle separately, it is more successful in compensating for the high brightness gradient in the image.

A complete set of observations in lines of heavy ions of the team of prof. Habbal from the 2010 TSE processed with the ACHF can be found in [aHDM11] – compare with Figure 3.4.

Even though the FNRGF was designed for images with relatively low signal to noise ratio, it can also be used for white-light images. The computation shown in Figure 3.10 takes only several seconds on current computers with the latest implementation of the FNRGF even though the

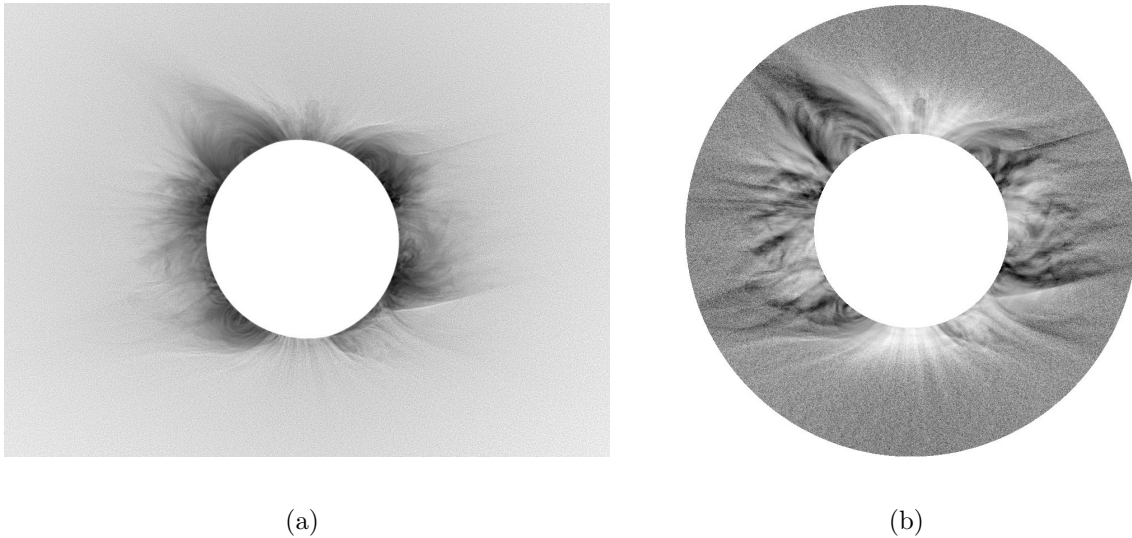


Figure 3.9: The same original image processed by ACHF (a) and FNRGF (b). The original image is an image of Fe XIV emission as observed by the team of prof. Habbal during the 2010 TSE. Figure (a) prepared for [aHDM11], in negative.

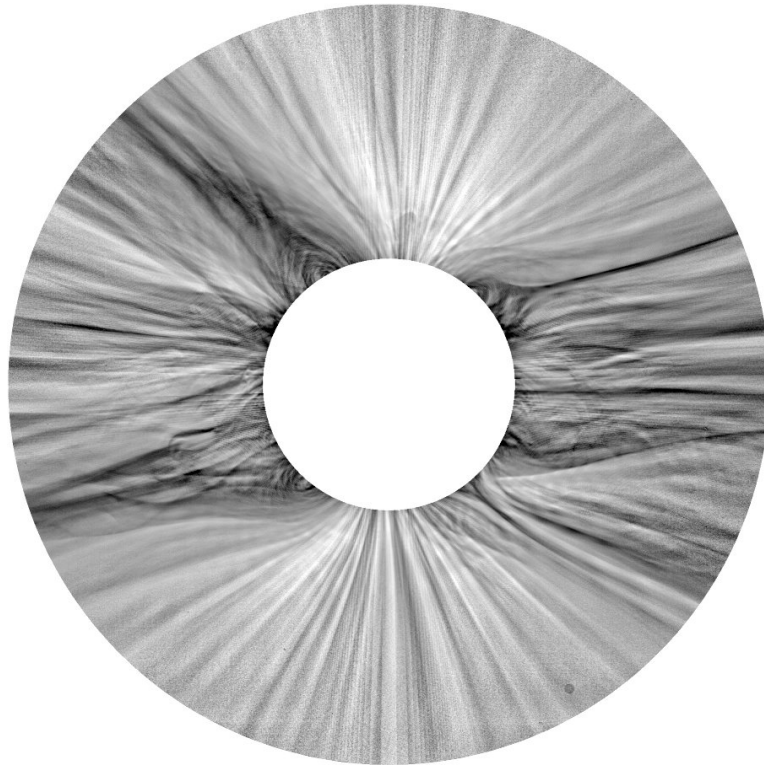
radius of the largest processed circle was about 900 pixels. This is at least an order of magnitude faster than enhancement of large-scale structures with the ACHF. However, the FNRGF can never enhance as fine details as the ACHF. It is an option to use the FNRGF for enhancement of the large-scale structures and the ACHF for fine details and then compose the results. The advantage of the FNRGF is higher contrast of the enhanced structures further from the Sun.

### 3.4 Software implementation

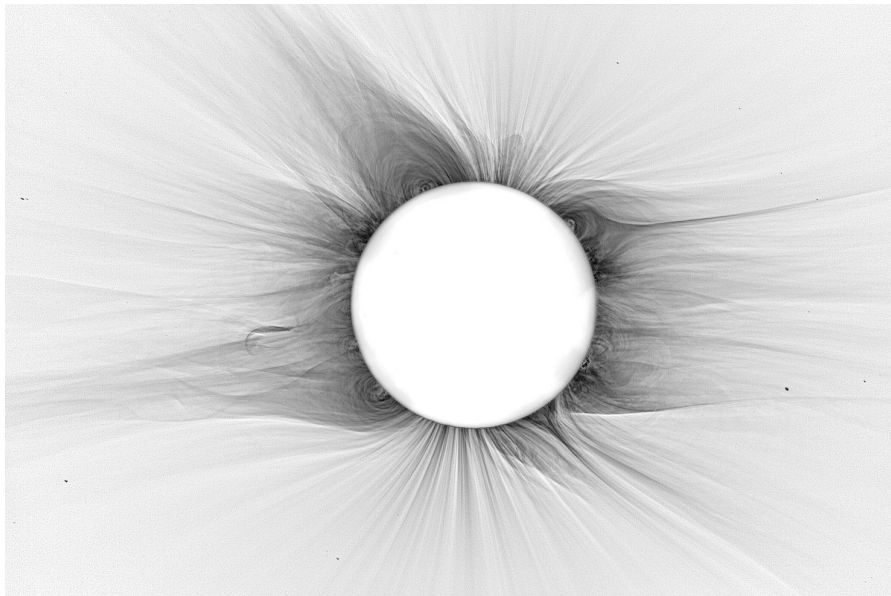
The FNRGF was first implemented in fall 2010 in the FNRGF software in Borland Delphi and later also by Huw Morgan in IDL (a standard scientific programming language used in astronomy, see <http://www.exelisvis.com/ProductsServices/IDL.aspx> for details) as part of the Solar Software CORIMP package. This has been completely recoded since spring 2013. The new version is much faster, which allows testing with various parameter settings. This has led to further improvements to the software and to the filter. More detailed images showing fainter and smaller structures can be enhanced.

The application can be run in Microsoft Windows operating systems and in Windows emulators (such as Wine for Linux).

A detailed description of the software implementation of the FNRGF – the FNRGF software – can be found in the full version of the doctoral thesis.



(a)



(b)

Figure 3.10: A white-light image of the inner corona as observed during the 2010 TSE by the team of prof. Habbal processed with the FNRGF (a) with 150 angular segments and attenuation coefficients  $A_k$  set to  $(1, 0.99, 0.98, \dots)$ ,  $C_k$  to  $(1, 0.98, 0.96, \dots)$  and with the ACHF (b), both images are shown in negative. Image (b) downloaded from [dDru10].

# 4 Conclusion

The short version of the doctoral thesis *Application of Adaptive Filters in Processing of Solar Corona Images* gives an introduction to solar corona imaging. The aim of the thesis was proposing, implementing and testing new filters suitable for images which contain more noise than regular white-light compositions of total solar eclipse images, i.e. images from coronagraphs, from cosmic probes in both visible and shorter-wavelength part of the spectrum and images taken during total solar eclipses in specific spectral lines.

The filter described above was proposed, implemented, and tested on various types of data. Many processed images can be found in the thesis. It is the Fourier-normalizing-radial-graded filter (FNRRGF), which is based on the nowadays commonly used Normalizing-radial-graded filter and has much higher adaptivity than this filter. The filter was published in [aDMH11] and after being fully recoded, the implementation was much faster; it enabled testing of various parameters and improvement of the filter to enhance even finer details than the original filter. The filter is a numerical method for enhancing coronal structures in images both from total solar eclipses and space-borne observations that is based on approximating the local brightness and contrast with attenuated trigonometric polynomials. The filter enables visualization of faint coronal structures in images with relatively low signal to noise ratio while compensating for both the steep decrease of brightness and contrast in the corona in the radial direction and also for the local changes of these quantities in the azimuthal direction. The processed images of emission from heavy ions during the 2010 total solar eclipse are nowadays the most detailed images showing the inner corona in spectral lines with a dominant radiative component in the visible wavelength range.

The doctoral thesis fulfills most of the goals set in the treatise.

# Bibliography

## Author's publications

- [aDru05] DRUCKMÜLLEROVÁ, Hana. A new numerical method for solar corona image processing. *I.A.P.P.P. Communications*. 2005, No. 99, pp. 1-4.
- [aDMH11] DRUCKMÜLLEROVÁ, Hana, Huw MORGAN, and Shadia R. HABBAL. ENHANCING CORONAL STRUCTURES WITH THE FOURIER NORMALIZING-RADIAL-GRADED FILTER. *The Astrophysical Journal*. 2011-08-20, Vol. 737, No. 2, pp. 88-97. ISSN 0004-637x. DOI: 10.1088/0004-637X/737/2/88. Available from: <http://stacks.iop.org/0004-637X/737/i=2/a=88?key=crossref.5dd91db1442b5fc7799beb6953ba19ff>
- [aHDM11] HABBAL, Shadia R., Miloslav DRUCKMÜLLER, Huw MORGAN, Adalbert DING, Judd JOHNSON, Hana DRUCKMÜLLEROVÁ, Adrian DAW, Martina ARNDT, Martin DIETZEL, and Jon SAKEN. THERMODYNAMICS OF THE SOLAR CORONA AND EVOLUTION OF THE SOLAR MAGNETIC FIELD AS INFERRED FROM THE TOTAL SOLAR ECLIPSE OBSERVATIONS OF 2010 JULY 11. *The Astrophysical Journal*. 2011, Vol. 734, No. 2, pp. 120-137. ISSN 0004-637x. DOI: 10.1088/0004-637X/734/2/120. Available from: <http://stacks.iop.org/0004-637X/734/i=2/a=120?key=crossref.7d305176173b49b98d661d855fa560b0>

## Scientifically less trusted references

Especially web links, listed to give a more complete overview of the topic.

- [bDru03] DRUCKMÜLLEROVÁ, Hana. *Počítačové zpracování obrazů sluneční korony*. Brno, 2003. Středoškolská odborná činnost. Gymnázium, Brno-Řečkovice. Supervisor Dalibor Kott.

## Other references

- [cBHK95] BRUECKNER, G. E., R. A. HOWARD, M. J. KOOMEN, C. M. KORENDYKE, D. J. MICHELS, J. D. MOSES, D. G. SOCKER, K. P. DERE, P. L. LAMY, A. LLEBARIA, M. V. BOUT, R. SCHWENN, G. M. SIMNETT, D. K. BEDFORD, and C. J. EYLES. The Large Angle Spectroscopic Coronagraph (LASCO). *Solar Physics*. 1995, Vol. 162, Issue 1-2, pp. 357-402. ISSN 0038-0938. DOI: 10.1007/BF00733434. Available from: <http://link.springer.com/10.1007/BF00733434>
- [cDru13] DRUCKMÜLLER, Miloslav. A NOISE ADAPTIVE FUZZY EQUALIZATION METHOD FOR PROCESSING SOLAR EXTREME

ULTRAVIOLET IMAGES. The Astrophysical Journal Supplement Series. 2013, vol. 207, issue 2, s. 25-29. DOI: 10.1088/0067-0049/207/2/25. Available from: <http://stacks.iop.org/0067-0049/207/i=2/a=25?key=crossref.7c1a4ee3e6e36dffddd5ce0b18daa7eb>

- [cDRM06] DRUCKMÜLLER, Miloslav, Vojtech RUŠIN, and Milan MINAROVJECH. A new numerical method of total solar eclipse photography processing. *Contributions of the Astronomical Observatory Skalnaté Pleso*. Vol. 36, No. 3, pp. 131-148. Available from: <http://adsabs.harvard.edu/abs/2006CoSka...36..131D>
- [cEsp00] ESPENAK, Fred. Digital Compositing Techniques for Coronal Imaging. In: LIVINGSTON, W. and Atila ÖZGÜÇ. *The last total solar eclipse of the millennium in Turkey*. San Francisco: Astronomical Society of the Pacific, 2000, pp. 101-112. ISBN 1-58381-032-3. Available from: <http://adsabs.harvard.edu/abs/2000ASPC...205..101E>
- [cGoP10] GOLUB, Leon and Jay M. PASACHOFF. The Solar Corona. 2nd edition. New York: Cambridge University Press, 2010, xiv, 390 pp. ISBN 05-218-8201-X.
- [cKKN88] KOUTCHMY, Olga, Serge KOUTCHMY, Christian NITSCHELM, Július SÝKORA, and Raymond N. SMARTT. Image processing of coronal pictures. In: *Solar and stellar coronal structure and dynamics: Proceedings of the Ninth Sacramento Peak Summer Symposium*. Altrock, R. C. Sunspot, NM, U.S.A.: National Solar Observatory, 1988, pp. 256-266. Available from: <http://adsabs.harvard.edu/abs/1988sscd.conf..256K>
- [cLiM83] LIKEŠ, Jiří and Josef MACHEK. *Matematická statistika*. 1st edition. Jarmila Novotná. Praha: SNTL - Nakladatelství technické literatury, n.p., 1983, 180 s. Matematika pro vysoké školy technické.
- [cLyo32] LYOT, Bernard. Étude de la couronne solaire en dehors des éclipses. Avec 16 figures dans le texte. *Zeitschrift für Astrophysik*. 1932, Vol. 5, pp. 73-95. Available from: <http://adsabs.harvard.edu/abs/1932ZA.....5...73L>
- [cMHW06] MORGAN, Huw, Shadia R. HABBAL, and Richard WOO. The Depiction of Coronal Structure in White-Light Images. *Solar Physics*. 2006, Vol. 236, No. 2, pp. 263-272. ISSN 0038-0938. DOI: 10.1007/s11207-006-0113-6. Available from: <http://www.springerlink.com/index/10.1007/s11207-006-0113-6>
- [cSta02] STAUNING, Peter. High-voltage power grid disturbances during geomagnetic storms. In: *Solspa 2001, Proceedings of the Second Solar Cycle and Space Weather Euroconference*. Huguette Sawaya-Lacoste. Vico Equense, Italy: Noordwijk: ESA Publications Division, 2002, pp. 521-524. ESA Special Publication, 477. ISBN 92-9092-749-6. Available from: [http://adsabs.harvard.edu/cgi-bin/nph-data\\_query?bibcode=2002ESASP.477..521S&link\\_type=ARTICLE&db\\_key=AST&high=](http://adsabs.harvard.edu/cgi-bin/nph-data_query?bibcode=2002ESASP.477..521S&link_type=ARTICLE&db_key=AST&high=)

## Scientifically less trusted references

Especially web links, listed to give a more complete overview of the topic.

- [dDru10] Corona up to 3.5 solar radii. DRUCKMÜLLER, Miloslav. *Eclipse Photography Homepage by Miloslav Druckmüller* [online]. 2010, 2010-09-27 [cit. 2014-03-18]. Available from: [http://www.zam.fme.vutbr.cz/~druck/eclipse/Ecl2010t/Tse2010t\\_1000mm\\_1/Hr/Tse2010t\\_wrr1.png](http://www.zam.fme.vutbr.cz/~druck/eclipse/Ecl2010t/Tse2010t_1000mm_1/Hr/Tse2010t_wrr1.png)
- [dGre12] GREEKGEEK. *If the Massive Solar Flare of 1859 (the "Carrington Flare") Happened Today...* [online]. 2012, 2012-11-10 [cit. 2012-12-28]. Available from: <http://greekgeek.hubpages.com/hub/massive-solar-flare-1859>
- [dVso13] *Virtual Solar Observatory* [online]. [cit. 2013-02-06]. Available from: <http://sdac.virtualsolar.org/cgi/search>

# Curriculum vitae

**Name:** Hana Druckmüllerová  
**Address:** Helfertova 7, Brno, 613 00, Czech Republic  
**Contact:** tel. (+420) 737 827 808, e-mail hanadruck@seznam.cz

## Education

from 2010 **Ph.D. student of Applied Mathematics** at Institute of Mathematics, Faculty of Mechanical Engineering, **Brno University of Technology** (IM FME BUT)  
2010-10 – 2011-01 as **Exchange visitor at Institute for Astronomy, University of Hawaii**, Honolulu, U.S.A.  
2005 – 2010 **Master degree (Ing.) and bachelor degree (Bc.)** in Mathematical Engineering at FME BUT  
2009-08/12 on **study stay** at Mathematical Sciences, **Chalmers University of Technology**, Gothenburg, Sweden

## Work experience

from 2014-01 **assistant lecturer** at IM FME BUT, teaching tutorials of Mathematics II and Applications of Fourier Analysis  
from 2010-06 **Ph.D. student** at IM FME BUT, teaching tutorials of Mathematics II, Mathematics II-B, Mathematics III, Computer Geometry and Graphics, and Applications of Fourier Analysis (newly introduced course)  
from 2013-01 **proof reader** for magazine Mensa of Mensa Czech Republic – volunteer member work  
from 2008-10 **Member of Senate** of FME BUT, 2008-10 – 2009-08 also **Chair of its Study committee**  
2009-01, 2012-01 **teaching computer classes** at grammar school EKO gymnázium Brno o.p.s., Labská 27

## Knowledge and skills

### Languages

mother tongue	<b>Czech</b>
proficient in	<b>English</b> (CAE from 2005-06)
limited proficiency	German
basic knowledge of	Russian, Swedish

### Computer skills

**Borland Delphi** programming language (Object Pascal), **L<sup>A</sup>T<sub>E</sub>X 2<sub>ε</sub>** typographic system, **Matlab** computational software **image processing: Adobe Photoshop, GIMP** and **SOFO ACC**, **MS Word**, **MS Excel**, **Open-Office.org Writer Math**, common-user knowledge of Windows and **Linux**-based operating systems

### Other skills

**driving licence** group B

## **Abstrakt**

Fotografování sluneční koróny patří mezi nejobtížnější úlohy astrofotografie a zároveň je jednou z klíčových metod pro studium koróny. Tato práce přináší ucelený souhrn metod pro její pozorování pomocí snímků. Práce obsahuje nutnou matematickou teorii, postup pro zpracování snímků a souhrn adaptivních filtrů pro vizualizaci koronálních struktur v digitálních obrazech. Dále přináší návrh nových metod určených především pro obrazy s vyšším obsahem šumu, než je běžné u obrazů bílé koróny pořízených během úplných zatmění Slunce, např. pro obrazy pořízené pomocí úzkopásmových filtrů. Fourier normalizing-radial-graded filter, který byl navržen v rámci této práce, je založen na aproximaci hodnot pixelů a jejich variability pomocí trigonometrických polynomů s využitím dalších vlastností obrazu.

## **Abstract**

Solar corona photography counts among the most complicated tasks in astrophotography. It also plays a key role for research of the solar corona. This thesis brings a complete overview of methods for imaging the solar corona. It contains the necessary mathematical background, the sequence of steps for image processing, an overview of adaptive filters used for visualization of corona structures in digital images, and new proposed methods. It is especially suited for images which contain more noise than it is typical for images of the white corona taken during total solar eclipses, e.g. images taken with narrow-band filters. The Fourier normalizing-radial-graded filter method that I proposed during my PhD study is based on approximation of pixel values and their variability with trigonometric polynomials using other properties of the image.